Radio Wave Propagation Along Mixed Paths Through a Four-Layered Model of Rain Forest: An Analytic Approach

Le-Wei Li, *Senior Member, IEEE*, Tat-Soon Yeo, *Senior Member, IEEE*, Pang-Shyan Kooi, *Member, IEEE*, and Mook-Seng Leong, *Member, IEEE*

***Abstract*—This paper presents a novel full-wave analysis of the radio waves that are excited from a dipole antenna located in the trunk layer and propagate inside a four-layered forest medium. The dyadic Green's functions for the four-layered geometry are applied first to derive the integral expression of the electric fields. The closed form of the electric fields is then obtained by using the quasi-static approximation, saddle-point technique, and branch-cut integrations in the complex plane and, hence, expressed in terms of direct waves, multiple reflected waves, and lateral waves. Two kinds of images, i.e., the quasi-dynamic and complex images, are considered in the integration in the complex plane. Among those waves excited by a dipole antenna in the four-layered medium, it is shown theoretically and numerically that the lateral wave along the upper-side air-canopy interface plays a role of dominant modes. Propagation mechanism of other lateral waves due to the air-canopy, canopy-trunk, and trunk-ground interfaces is also discussed and analyzed so as to gain an insight into the wave characteristics. Transmission losses of the lateral waves are calculated numerically.**

***Index Terms*—Antenna radiation, dyadic Green's function, inhomogeneous stratified media, radio propagation terrain factors, radio wave propagation.**

I. Introduction

FOREST foliage and other vegetation significantly restrict the communication range when the radio waves propagate through the vegetation. Quantitively detailed knowledge of the radio wave propagation mechanism and radio transmission loss is essential for designing the communication link. It is also useful to assess the effects of the forest on the digital-spectrum of radio communication systems.

To investigate the radio attenuation due to the forest environment, a semi-infinitely extended vegetation above a semi-infinite ground [1]–[6] and a foliage layer between a semi-infinite free-space and semi-infinite ground [7]–[9] had been used earlier for the sake of mathematical simplicity. Recently, a four-layered geometry (as shown in Fig. 1) has been widely adopted as a typical forest model and commonly used in the analysis of the transmission loss of radio waves propagating through the forest [10]–[14].

Manuscript received June 11, 1996; revised November 6, 1997. This work was supported in part by a grant under the NUS/Telecoms Joint R&D Project 018.

The authors are with Communications and Microwave Division, Department of Electrical Engineering, National University of Singapore, Singapore 119260.

Publisher Item Identifier S 0018-926X(98)05790-1.

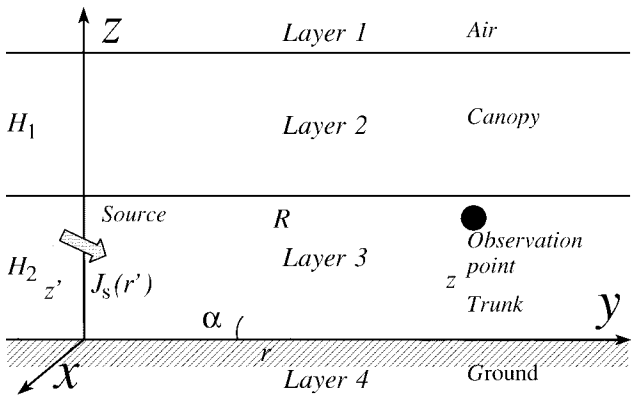

Fig. 1. Geometry of the problem.

In this geometry, the first region (layer I) is the semi-infinite free-space. The second region (layer II) represents the forest canopy, while the third region (layer III) models the trunk layer of the forest. The last region (layer IV) is the semi-infinite ground plane. This model was proposed in 1983 by Cavalcante *et al.* [10], analyzed by Lian [11] and by Li and Jiao [12], both in 1986, and used by Seker and Schneider [13] in 1987 and by Seker [14] in 1989. The model has been adopted for analyzing very high frequency (VHF) and ultrahigh frequency (UHF) radio waves propagation through and scattering by the forest foliage by Li [15]. In this paper, it is assumed as in the work by Cavalcante *et al.* [10] that all the layers are isotropic and homogeneous. To solve the problem, the full-wave theory via the spectral domain dyadic Green's function technique is applied because of: 1) the guaranteed accuracy and good exponential convergence; 2) the spatial coordinate flexibility by means of the dyadic Green's function; and 3) an arbitrary current distribution in the isotropic and/or anisotropic media.

As the distance between the transmitter and the receiver is very long, the radio wave propagation through the stratified forest is characterized by the lateral wave that mainly propagates upside along the air-canopy interface. The extensively detailed investigation and comprehensive discussion on the mechanism, property, and derivation of lateral waves can be found in the specialized monograph written by King, Owens and Wu [16]. Other investigations relevant to the lateral waves in the planar geometry can also be found from the literature

such as those by Wu and King, i.e., [17], [18], Pan [19], and Dunn [20].

For the short distance, however, such a propagation is dominated by the direct wave and modified by the several hop-reflected waves. In this paper, the direct and reflected fields radiated from the real dipole antenna and its images (including the quasi-dynamic images and complex images) in the four-layer stratified model are derived in closed form. Also, the lateral waves propagating along the interfaces I, II, and III are obtained and expressed in closed form. Both horizontal and vertical polarizations of the dipole are considered. For the communications inside the forest, the distance between transmitter and receiver is much larger than the wavelength so that the fields in the stratified structure are described by only the lateral wave on the air side along the air-canopy interface. Transmission losses of the waves are also computed by using the field configuration developed.

II. The Integral Equation

A. Solution in Vector Form

The model considered here is shown in Fig. 1. Layer 3 extending from $z = 0$ to $z = H_2$, represents a medium of tree trunks that has a permittivity ε_3, a conductivity σ_3, and a permeability μ. Layer 2, extending from $z = H_2$ to $z = H_1 + H_2$, represents a medium of tree crowns (canopy) with dielectric parameters ε_2, σ_2, and μ_2. The region $z \geq H_1 + H_2$ (or layer 1) corresponds to semi-infinite free-space with parameters ε_0, σ, and μ. The region $z \leq 0$ (or layer 4) denotes a (nonperfectly) conducting flat earth with parameters ε_4, σ_4, and μ_4.

The electric dipole with an inclination angle α with respect to the boundary plane between layers is located in the third layer (medium 3), as shown in Fig. 1, and the observation point is also located in the third layer (medium 3). The electromagnetic fields are assumed to have a time dependence of $\exp(-j\omega t)$. The parameters of medium i ($i = 1, 2, 3$ or 4) are generally expressed as ε_i, σ_i, and μ_i. Thus, the wave number k_i satisfies $k_i^2 = \omega^2\epsilon_i\mu_i(1+(j\sigma_i/\omega\epsilon_i))$. The magnetic permeability μ_i of each layer is assumed to be equal to the permeability μ_0 in free-space.

The current distribution of an electric dipole with an inclination angle α with respect to the ground plane, as shown in Fig. 1, may be expressed as

$$\begin{aligned}\boldsymbol{J}_3(\boldsymbol{r}') &= (P_x\hat{\boldsymbol{x}} + P_z\hat{\boldsymbol{z}})\delta(x')\delta(y')\delta(z'-z_0)\\ &= [P_x(\cos\phi'\hat{\boldsymbol{r}} - \sin\phi'\hat{\boldsymbol{\phi}}) + P_z\hat{\boldsymbol{z}}]\\ &\quad\cdot\frac{\delta(r')\delta(z'-z_0)}{2\pi r'}\end{aligned} \tag{1}$$

where $z_0 = z'$ is the height of the dipole (subsequently we will use z' to replace the source point z_0) and P_x and P_z are the horizontal and vertical dipole moments, respectively. Using the dyadic Green's function published recently by Li *et al.* [21] for the four-layered planar geometry, we derive the integral solution of the radiative fields as follows for the regions 1) $z' \leq z \leq H_2$

$$\begin{aligned}\boldsymbol{E}_3^{>}(\boldsymbol{r}) = -\frac{\omega\mu_0}{4\pi}\int_0^\infty \frac{d\lambda}{h_3}\,[P_x\{[(1+\mathcal{A}_M^{33})\boldsymbol{M}_{o1\lambda}(h_3)\\ +\mathcal{C}_M^{33}\boldsymbol{M}_{o1\lambda}(-h_3)]e^{-jh_3z'} + [\mathcal{B}_M^{33}\boldsymbol{M}_{o1\lambda}(h_3)\\ +\mathcal{A}_M^{33}\boldsymbol{M}_{o1\lambda}(-h_3)]e^{jh_3z'} - \frac{jh_3}{k_3}\,[(1+\mathcal{A}_N^{33})\\ \times\boldsymbol{N}_{e1\lambda}(h_3) + \mathcal{C}_N^{33}\boldsymbol{N}_{e1\lambda}(-h_3)]e^{-jh_3z'}\\ +\frac{jh_3}{k_3}\,[\mathcal{B}_N^{33}\boldsymbol{N}_{e1\lambda}(h_3) + \mathcal{A}_N^{33}\boldsymbol{N}_{e1\lambda}(-h_3)]\\ \times e^{jh_3z'}\} + \frac{P_z\lambda}{k_3}\,\{[(1+\mathcal{A}_N^{33})\boldsymbol{N}_{e0\lambda}(h_3)\\ +\mathcal{C}_N^{33}\boldsymbol{N}_{e0\lambda}(-h_3)]e^{-jh_3z'} + [\mathcal{B}_N^{33}\boldsymbol{N}_{e0\lambda}(h_3)\\ +\mathcal{A}_N^{33}\boldsymbol{N}_{e0\lambda}(-h_3)]e^{jh_3z'}\}]\end{aligned} \tag{2a}$$

and 2) $0 \leq z \leq z'$,

$$\begin{aligned}\boldsymbol{E}_3^{<}(\boldsymbol{r}) = -\frac{\omega\mu_0}{4\pi}\int_0^\infty \frac{d\lambda}{h_3}\,[P_x\{[\mathcal{A}_M^{33}\boldsymbol{M}_{o1\lambda}(h_3)\\ +\mathcal{C}_M^{33}\boldsymbol{M}_{o1\lambda}(-h_3)]e^{-jh_3z'} + [\mathcal{B}_M^{33}\boldsymbol{M}_{o1\lambda}(h_3)\\ +(1+\mathcal{A}_M^{33})\boldsymbol{M}_{o1\lambda}(-h_3)]e^{jh_3z'} - \frac{jh_3}{k_3}\,[\mathcal{A}_N^{33}\\ \times\boldsymbol{N}_{e1\lambda}(h_3) + \mathcal{C}_N^{33}\boldsymbol{N}_{e1\lambda}(-h_3)]e^{-jh_3z'}\\ +\frac{jh_3}{k_3}\,[\mathcal{B}_N^{33}\boldsymbol{N}_{e1\lambda}(h_3) + (1+\mathcal{A}_N^{33})\boldsymbol{N}_{e1\lambda}(-h_3)]\\ \times e^{jh_3z'}\} + \frac{P_z\lambda}{k_3}\,\{[\mathcal{A}_N^{33})\boldsymbol{N}_{e0\lambda}(h_3)\\ +\mathcal{C}_N^{33}\boldsymbol{N}_{e0\lambda}(-h_3)]e^{-jh_3z'} + [\mathcal{B}_N^{33}\boldsymbol{N}_{e0\lambda}(h_3)\\ +(1+\mathcal{A}_N^{33})\boldsymbol{N}_{e0\lambda}(-h_3)]e^{jh_3z'}\}]\end{aligned} \tag{2b}$$

where $h_i = \sqrt{k_i^2 - \lambda^2}$ ($i = 1, 2, 3$ and 4), the coefficients $\mathcal{A}_{M,N}^{33}$, $\mathcal{B}_{M,N}^{33}$, and $\mathcal{C}_{M,N}^{33}$ of dyadic Green's functions for the planar four-layered media are expressed by Li *et al.* [21] and will not be given here for the sake of saving space and the superscripts $>$ and $<$ denote the regions where $0 \leq z \leq z'$ and $z' \leq z \leq H$ in the layer III.

In (2a) and (b), the symmetry of the expression with respect to the field and source points, $\boldsymbol{r}$, and $\boldsymbol{r}'$ has been used. Also

$$\begin{aligned}\lim_{r\to 0}\frac{J_1(\lambda r)}{\lambda r} &= \frac{1}{2}\\ \left.\frac{dJ_1(\lambda r)}{d(\lambda r)}\right|_{r=0} &= \frac{1}{2}\\ J_0(\lambda r)|_{r=0} &= 1\end{aligned} \tag{3}$$

have been employed in the integration. The vector wave functions in explicit form are given by

$$\begin{aligned}\boldsymbol{M}_{on\lambda}(h) &= \boldsymbol{\nabla}\times[J_n(\lambda r)\sin(n\phi)e^{jhz}\hat{\boldsymbol{z}}]\\ &= \left[\frac{nJ_n(\lambda r)}{r}\cos(n\phi)\hat{\boldsymbol{r}}\right.\\ &\quad\left.-\frac{\partial J_n(\lambda r)}{\partial r}\sin(n\phi)\hat{\boldsymbol{\phi}}\right]e^{jhz}\end{aligned} \tag{4a}$$

$$\boldsymbol{N}_{en\lambda}(h) = \frac{1}{\sqrt{\lambda^2+h^2}}\,\nabla\times\nabla\times[J_n(\lambda r)\cos(n\phi)e^{jhz}\hat{\boldsymbol{z}}]$$
$$= \frac{1}{\sqrt{\lambda^2+h^2}}\left[jh\,\frac{\partial J_n(\lambda r)}{\partial r}\,\cos(n\phi)\hat{\boldsymbol{r}} - \frac{jnh}{r}\,J_n(\lambda r)\sin(n\phi)\hat{\boldsymbol{\phi}} + \lambda^2 J_n(\lambda r)\cos(n\phi)\hat{\boldsymbol{z}}\right]e^{jhz}. \tag{4b}$$

B. $\hat{\boldsymbol{z}}$ Component of the Fields

Equation (2) represents in vector form the radiated field due to the dipole antenna and, therefore, it consists of full components of the electric field. However, only the $\hat{\boldsymbol{z}}$ components of (2a) and (b) are relatively important, not only because the vertical receiver is frequently used in the measurement, but also because the length of the paper is limited. Therefore, we shall consider only the $\hat{\boldsymbol{z}}$ component of the fields subsequently. The other components can be obtained and evaluated in a similar fashion.

Substituting the coefficients of the scattering dyadic Green's functions in [21] into (2) and taking the $\hat{\boldsymbol{z}}$ component of cylindrical vector wave functions we have

$$\begin{bmatrix}E_{3z}^{>}\\ E_{3z}^{<}\end{bmatrix} = \frac{j\omega\mu_0}{4\pi k_3^2}\int_0^\infty \frac{\lambda^2 d\lambda}{D_3^V}\left(P_x\cos\phi J_1(\lambda r)\begin{bmatrix}\Phi_+^{>}(\lambda)\\ \Phi_+^{<}(\lambda)\end{bmatrix} + jP_z\,\frac{\lambda J_0(\lambda r)}{h_3}\begin{bmatrix}\Phi_-^{>}(\lambda)\\ \Phi_-^{<}(\lambda)\end{bmatrix}\right) \tag{5}$$

where

$$\Phi_\pm^{>}(\lambda) = [1\pm R_3^V e^{j2h_3z'}]\{[1+R_1^V R_2^V e^{j2h_2H_1}] + [R_2^V + R_1^V e^{j2h_2H_1}]e^{j2h_3(H_2-z)}\}e^{jh_3(z-z')} \tag{6a}$$

$$\Phi_\pm^{<}(\lambda) = [1- R_3^V e^{j2h_3z}]\{\mp[1+R_1^V R_2^V e^{j2h_2H_1}] + [R_2^V + R_1^V e^{j2h_2H_1}]e^{j2h_3(H_2-z')}\}e^{jh_3(z'-z)} \tag{6b}$$

$$D_3^V = 1 + R_1^V R_2^V e^{j2h_2H_1} + [R_2^V + R_1^V e^{j2h_2H_1}]\times R_3^V e^{j2h_3H_2}. \tag{6c}$$

In (6), R_1^V, R_2^V, and R_3^V are the reflection coefficients for vertical polarized waves given below:

$$R_1^V = \frac{k_2^2h_1 - k_1^2h_2}{k_2^2h_1 + k_1^2h_2} \tag{7a}$$

$$R_2^V = \frac{k_3^2h_2 - k_2^2h_3}{k_3^2h_2 + k_2^2h_3} \tag{7b}$$

$$R_3^V = \frac{k_4^2h_3 - k_3^2h_4}{k_4^2h_3 + k_3^2h_4}. \tag{7c}$$

The integrals of $\hat{\boldsymbol{z}}$ components consist of two terms that are proportional to the vertical dipole moment P_z or the horizontal dipole moment P_x, respectively. Since

$$J_n(-\lambda r) = (-1)^n J_n(\lambda r), \qquad n = 0,1,2,\cdots \tag{8}$$

so the Bessel functions of $J_0(\lambda r)$ and $J_1(\lambda r)$ need to be transformed to the Hankel functions $H_0^{(1)}(\lambda r)$ and $H_1^{(1)}(\lambda r)$ in order to calculate conveniently the integral (5). The z components of the radiative electric field excited by the horizontal and vertical moments can be obtained from

$$\begin{bmatrix}E_{3z}^{>}\\ E_{3z}^{<}\end{bmatrix} = \frac{j\omega\mu_0P_x}{8\pi k_3^2}\,\cos\phi\int_{-\infty}^{\infty}\begin{bmatrix}\Phi_+^{>}(\lambda)\\ \Phi_+^{<}(\lambda)\end{bmatrix}H_1^{(1)}(\lambda r)\,\frac{\lambda^2 d\lambda}{D_3^V} - \frac{\omega\mu_0P_z}{8\pi k_3^2}\int_{-\infty}^{\infty}\begin{bmatrix}\Phi_-^{>}(\lambda)\\ \Phi_-^{<}(\lambda)\end{bmatrix}H_0^{(1)}(\lambda r)\,\frac{\lambda^3 d\lambda}{h_3D_3^V}. \tag{9}$$

To derive the far-zone field in closed form, we use the asymptotic form of the Hankel functions expressed by

$$H_0^{(1)}(\lambda r) = \sqrt{\frac{2}{\pi\lambda r}}\,e^{j(\lambda r-(\pi/4)} \tag{10a}$$

$$H_1^{(1)}(\lambda r) = \sqrt{\frac{2}{\pi\lambda r}}\,e^{j(\lambda r-(3\pi/4)}. \tag{10b}$$

The large argument condition is almost always satisfied in this case under consideration. In fact, as to be discussed later on, this integral is dominated by the values at the pole points where $\lambda = k_1 = k_0$ (for the lateral wave along upper side of the air-canopy interface), k_2 (for the lateral wave along upper side of the canopy-trunk interface), k_3 (for the direct wave and multireflected waves), and k_4 (for the lateral wave along upper side of the trunk-ground interface). In this paper, the frequency used here is about 100 MHz or above. Therefore, the term $k_0r = 2\pi 100\times 10^6/(3\times 10^8)r = 2.094r$ or above. As the transmitter–receiver distance is very large (at least the thickness of the forest layer, i.e., 20 m), λr is about 41.88, which is very much greater than one.

The denominator in the formulas (5) and (9) can be expressed using: 1) the Taylor expansion and 2) the binomial expansion together with 1) in following forms:

$$\frac{1}{D_3^V} = \sum_{m=0}^{\infty}[(R_2^V + R_1^V e^{j2h_2H_1})R_3^V e^{j2h_3H_2} + R_1^V R_2^V e^{j2h_2H_1}]^m. \tag{11}$$

For the sake of convenience, we separate the field E into two parts E^H and E^V due to the contributions of horizontal and vertical dipole moments, respectively. Using the complex transformation $\lambda = k_3\sin\beta$, (9) can be written as

$$\begin{bmatrix}E_{3z}^{>V}\\ E_{3z}^{<V}\end{bmatrix} = -\frac{\omega\mu_0k_3P_z}{8\pi}\sqrt{\frac{2}{\pi k_3r}}\,e^{-j(\pi/4)}\sum_{m=0}^{\infty}\begin{bmatrix}\mathcal{L}_3^{>}(m)\\ \mathcal{L}_3^{<}(m)\end{bmatrix} \tag{12a}$$

$$\begin{bmatrix}E_{3z}^{>H}\\ E_{3z}^{<H}\end{bmatrix} = \frac{\omega\mu_0k_3}{8\pi}\,P_x\cos\phi\sqrt{\frac{2}{\pi k_3r}}\,e^{-j(\pi/4)}\sum_{m=0}^{\infty}\begin{bmatrix}\mathcal{K}_3^{>}(m)\\ \mathcal{K}_3^{<}(m)\end{bmatrix} \tag{12b}$$

where

$$\begin{bmatrix}\mathcal{L}_3^{>}(m)\\ \mathcal{L}_3^{<}(m)\end{bmatrix} = \int_{\Gamma_0} d\beta e^{jk_3r\sin\beta}\sin^{5/2}\beta\begin{bmatrix}\Phi_-^{>}(\lambda)\\ \Phi_-^{<}(\lambda)\end{bmatrix} \times[(R_2^V + R_1^V e^{j2H_1\sqrt{k_2^2-k_3^2\sin^2\beta}})R_3^V \times e^{j2H_2k_3\cos\beta} + R_1^V R_2^V e^{j2H_1\sqrt{k_2^2-k_3^2\sin^2\beta}}]^m \tag{13a}$$

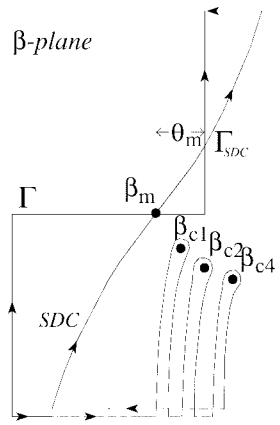

Fig. 2. The branch-cut (BC) integrations and the steepest descent contour (SDC) in complex β plane. The BC's and SDC together with the original path Γ_0 form a closed loop for which the residue is zero since the integrand function is analytical within the loop.

$$\begin{bmatrix}\mathcal{K}_3^{>}(m)\\ \mathcal{K}_3^{<}(m)\end{bmatrix} = \int_{\Gamma_0} d\beta e^{jk_3 r\sin\beta}\sin^{3/2}\beta\cos\beta \begin{bmatrix}\Phi_+^{>}(\lambda)\\ \Phi_+^{<}(\lambda)\end{bmatrix} \times [(R_2^V + R_1^V e^{j2H_1\sqrt{k_2^2-k_3^2\sin^2\beta}})R_3^V \times e^{j2H_2k_3\cos\beta} + R_1^V R_2^V e^{j2H_1\sqrt{k_2^2-k_3^2\sin^2\beta}}]^m. \quad (13b)$$

Γ_0 in (13) is the integral contour shown in [22, p. 454, Fig. 15-4]. Equations (13a) and (b) can be integrated by means of the saddle-point evaluation and branch-cut evaluations.

III. Quasi-Dynamic Images: Quasi-Static Approach and Saddle-Point Method

In this section, we will consider the radiated fields in the near-field region first. So the contribution of direct waves due to the real dipole antenna and the contributions of the reflected waves due to its images in the four-layered dielectric medium will be found. In the near zone, the field proportional to R^{-1} is the dominant wave, thus, we will conduct the *saddle-point* evaluation to obtain all the images from the integral.

To obtain the solution of the integral in (12), (13) must be evaluated first and there is no straightforward way. Examining the denominator in (11), we found [22] that there are three poles corresponding to $h_i = 0$ ($i = 1, 2$ and 4) because $h_i = \sqrt{k_i^2 - k_3^2\sin^2\beta}$ in (5), together with (6) and (7), is not a single-valued function of β, but h_3 is. Consider the enclosed loop in Fig. 2. Then, it is found that the residue of the enclosed integral is zero since the integrand function within the enclosed region is analytical. Hence, the integral in (13) consists of contributions from the steepest descent path and three branch cuts around the three poles.

To evaluate the integral along the steepest descent contour, the saddle-point technique is a direct method. However, the condition of the saddle-point technique (i.e., $kR \gg 1$) or the condition of the Hankel functions in far zone must hold. As shown earlier, the condition is almost always satisfied for the case considered in the paper.

Even so, we still desire to obtain a very accurate result by including all the contributions (although some are little) into the solution. To improve the accuracy of the solution, the integral evaluation should be modified by the quasi-static approximation. According to the conclusion drawn previously by Chow *et al.* [23] and by Aksun and Mittra [24] for the analysis of microstrip antennas, quasi-static approximation together with saddle-point technique produces the quasi-dynamic (or quasi-static) images. These quasi-dynamic images contribute to the dominant field distribution in the near zone.

A. Quasi-Static Approximation

Quasi-static approach approximates the Sommerfeld integral by exponential forms as $k_i \to 0$. The quasi-static fields contributed by the quasi-dynamic images are defined in the range where the distance between receiver and transmitter is much smaller than the free-space wavelength. Therefore, subtraction of these quasi-static terms from the Sommerfeld identity makes the remaining integrands decay faster. The asymptotic terms of the reflection coefficients $R_{1,2,3}^V$ in (7) then reduce to

$$\mathcal{R}_1^s = \frac{1-\epsilon_{2r}}{1+\epsilon_{2r}} \quad (14a)$$

$$\mathcal{R}_2^s = \frac{\epsilon_{2r}-\epsilon_{3r}}{\epsilon_{2r}+\epsilon_{3r}} \quad (14b)$$

$$\mathcal{R}_3^s = \frac{\epsilon_{4r}-\epsilon_{3r}}{\epsilon_{4r}+\epsilon_{3r}}. \quad (14c)$$

Thus, the integrals are rewritten as follows:

$$\begin{bmatrix}\mathcal{L}^{>}(m)\\ \mathcal{K}^{>}(m)\end{bmatrix} = \int_{\Gamma_0} d\beta\, e^{jk_3 r\sin\beta + jk_3(2H_2 - z - z')\cos\beta} \times \begin{bmatrix}\sin^{5/2}\beta\\ \sin^{3/2}\beta\end{bmatrix}(1 \mp \mathcal{R}_3^s e^{j2k_3 z'\cos\beta}) \times [(\mathcal{R}_2^s + \mathcal{R}_1^s e^{j2H_1\sqrt{k_2^2-k_3^2\sin^2\beta}}) + (1 + \mathcal{R}_1^s\mathcal{R}_2^s e^{j2H_1\sqrt{k_2^2-k_3^2\sin^2\beta}}) \times e^{j2k_3(z-H_2)\cos\beta}][\mathcal{R}_3^s(\mathcal{R}_2^s + \mathcal{R}_1^s \times e^{j2H_1\sqrt{k_2^2-k_3^2\sin^2\beta}})e^{j2H_2k_3\cos\beta} + \mathcal{R}_1^s\mathcal{R}_2^s e^{j2H_1\sqrt{k_2^2-k_3^2\sin^2\beta}}]^m. \quad (15)$$

Since the integrals $\mathcal{L}^{<}(m)$ and $\mathcal{K}^{<}(m)$ can be obtained from $\mathcal{L}^{>}(m)$ and $\mathcal{K}^{>}(m)$ by simply exchanging the position of z and z', only one set of the formulas in (13) is rewritten here in (15) to save space.

B. Direct and Multireflected Waves

In this paper, the direct wave due to the real dipole antenna and the reflected waves due to its dipole images are of interest. As shown in Fig. 2, we will first carry out the saddle-point integral evaluation along the steepest descent paths.

It is assumed that the horizontal distance r is so large that the saddle point can be shown as

$$\beta_m = \frac{\pi}{2} - \theta_m$$

where

$$\theta_m \simeq \arccos\left(\frac{r}{\mathcal{P}}\right), \qquad (m = 0, 1, 2, \cdots)$$

and $\mathcal{P}$ depending upon the propagation (via reflection) paths takes the form of one of the four definitions of R_+, R_-, R'_+, and R'_-, as given by (17). In Fig. 2, the point β_m on the complex plane is assumed. However, it should be pointed out that many saddle- points $(m = 0, 1, 2, \cdots)$ have been considered.

Generally, m is nonzero for the higher order reflected waves. Consider the integral path along Γ_{SDC}, which is the steepest descent path through β_m (see Fig. 2 for the path). If r is large enough, θ_m can be assumed to be nearly zero. By using the integral formula from the saddle-point method, it is found that $\mathcal{K}_3^{>}(m)$ and $\mathcal{K}_3^{<}(m)$ are relatively smaller than $\mathcal{L}_3^{>}(m)$ and $\mathcal{L}_3^{<}(m)$. The asymptotic field components $E_{3z}^{>V}$ and $E_{3z}^{>H}$ in (12) are obtained as follows:

$$\begin{aligned} E_{3z,qd}^{>V} = & -\frac{\omega\mu_0 P_z}{4\pi}\sqrt{\frac{k_3}{|k_3|}}\, e^{-j(5\pi/8)} \\ & \times \sum_{m=0}^{\infty}\Bigg[(1+\mathcal{R}_1^s\mathcal{R}_2^s e^{j2\sqrt{k_2^2-k_3^2}H_1}) \\ & \times \frac{e^{jk_3R'_-(m,z,z')}}{\sqrt{rR'_-(m,z,z')}} + (\mathcal{R}_2^s + \mathcal{R}_1^s e^{j2\sqrt{k_2^2-k_3^2}H_1}) \\ & \times \frac{e^{jk_3R_-(m,z,z')}}{\sqrt{rR_-(m,z,z')}} - \mathcal{R}_3^s(\mathcal{R}_2^s + \mathcal{R}_1^s e^{j2\sqrt{k_2^2-k_3^2}H_1}) \\ & \times \frac{e^{jk_3R_+(m,z,z')}}{\sqrt{rR_+(m,z,z')}} - \mathcal{R}_3^s(1+\mathcal{R}_1^s\mathcal{R}_2^s e^{j2\sqrt{k_2^2-k_3^2}H_1}) \\ & \times \frac{e^{jk_3R'_+(m,z,z')}}{\sqrt{rR'_+(m,z,z')}}\Bigg][\mathcal{R}_3^s(\mathcal{R}_2^s + \mathcal{R}_1^s e^{j2\sqrt{k_2^2-k_3^2}H_1}) \\ & + \mathcal{R}_1^s\mathcal{R}_2^s e^{j2\sqrt{k_2^2-k_3^2}H_1}]^m \end{aligned} \tag{16a}$$

$$\begin{aligned} E_{3z,qd}^{>H} = & \frac{\omega\mu_0 P_x\cos\phi}{4\pi}\sqrt{\frac{k_3}{|k_3|}}\, e^{-j(5\pi/8)} \\ & \times \sum_{m=0}^{\infty}\Bigg[(1+\mathcal{R}_1^s\mathcal{R}_2^s e^{j2\sqrt{k_2^2-k_3^2}H_1}) \\ & \times \frac{|2mH_2+z-z'|}{r}\,\frac{e^{jk_3R'_-(m,z,z')}}{\sqrt{rR'_-(m,z,z')}} \\ & + (\mathcal{R}_2^s + \mathcal{R}_1^s e^{j2\sqrt{k_2^2-k_3^2}H_1})\,\frac{|2(m+1)H_2-z-z'|}{r} \\ & \times \frac{e^{jk_3R_-(m,z,z')}}{\sqrt{rR_-(m,z,z')}} + \mathcal{R}_3^s(\mathcal{R}_2^s + \mathcal{R}_1^s e^{j2\sqrt{k_2^2-k_3^2}H_1}) \\ & \times \frac{|2(m+1)H_2-z+z'|}{r}\,\frac{e^{jk_3R_+(m,z,z')}}{\sqrt{rR_+(m,z,z')}} \\ & + \mathcal{R}_3^s \times (1+\mathcal{R}_1^s\mathcal{R}_2^s e^{j2\sqrt{k_2^2-k_3^2}H_1}) \\ & \cdot \frac{|2mH_2+z+z'|}{r}\Bigg] \\ & \times \frac{e^{jk_3R'_+(m,z,z')}}{\sqrt{rR'_+(m,z,z')}}[\mathcal{R}_3^s(\mathcal{R}_2^s + \mathcal{R}_1^s e^{j2\sqrt{k_2^2-k_3^2}H_1}) \\ & + \mathcal{R}_1^s\mathcal{R}_2^s e^{j2\sqrt{k_2^2-k_3^2}H_1}]^m \end{aligned} \tag{16b}$$

where

$$R_\pm(m,z,z') = \sqrt{r^2+[2(m+1)H_2 - z \pm z']^2} \tag{17a}$$

$$R'_\pm(m,z,z') = \sqrt{r^2+(2mH_2+z\pm z')^2}. \tag{17b}$$

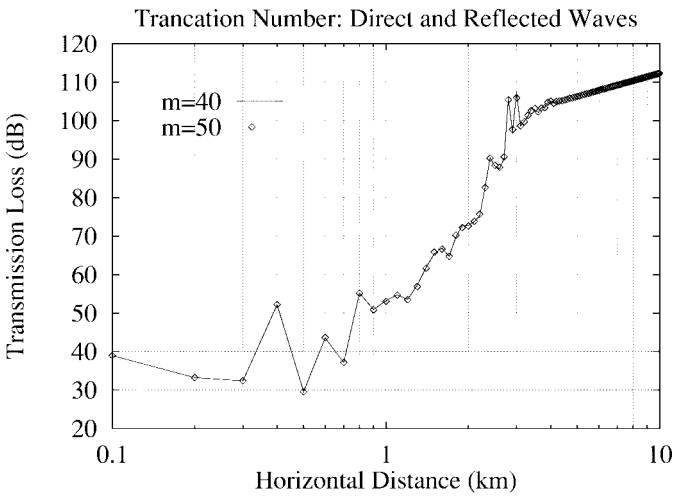

Fig. 3. Consideration of iteration convergence for the direct and multireflected waves.

From this consideration, it is seen that both β_m and θ_m are real numbers and should therefore be located on the real axis of the complex plane. Both $\hat{\boldsymbol{x}}$ and $\hat{\boldsymbol{z}}$ polarizations of the dipole have been taken into account in (16). The field components $E_{3z}^{<V}$ and $E_{3z}^{<H}$ can be obtained in a similar fashion. It has exactly the same form as (A.1) in the appendix except that the observation and source locations must be changed from (z, z') to (z', z).

C. Convergence Consideration

Numerical results demonstrate that the direct wave is still the major contribution to the overall guided waves, i.e., the direct and multireflected waves. However, the reflected waves play an important role as well in the overall guided waves and cannot definitely be neglected.

The convergence of the above iteration for direct wave and multireflected waves is examined numerically to demonstrate the contribution of the multireflected waves. Fig. 3 shows the transmission loss of the direct and multireflected waves at a frequency of 100 MHz against the horizontal distance r ranging from 0.1 to 10 km. Two cases are considered where the iteration truncation numbers (m) are 40 and 50. It is seen that to use $m = 40$ and $m = 50$ as truncation numbers actually gives the same results. Therefore, in the numerical computation, we considered the iteration up to $m = 40$, which is, in fact, the minimum truncation number for the iteration with a relative error of 0.877%. The formula of transmission loss concerned is given later.

IV. Lateral Waves: Branch-Cut Integrals

As shown earlier in (7), there are three branch points $h_1 = 0$, $h_2 = 0$, and $h_4 = 0$ (as illustrated in Fig. 2) corresponding to the lateral waves propagating along the air–canopy, canopy–trunk, and ground–trunk interfaces, respectively. Let

$$n_1 = k_1/k_3, \quad n_2 = k_2/k_3, \quad \text{and} \quad n_4 = k_4/k_3.$$

Thus, the branch points are located, respectively, at

$$\sin\beta_{c1} = n_1, \quad \sin\beta_{c2} = n_2, \quad \text{and} \quad \sin\beta_{c4} = n_4.$$

Since n_1 (representing the free-space) is smaller than unity and n_4 is larger than unity, the branch cut at β_{c1} plays an important role in the evaluation of the integration while the branch point β_{c4} has little effect on the radiowave propagation in the guide structure. n_2 is sometimes larger than unity and sometimes smaller than unity, depending upon the forest type. If n_2 is smaller than unity, the branch cut at β_{c2} will contribute significantly (otherwise, very litte) to the total far field.

A. Lateral Wave Along Air–Canopy Interface

The lateral wave comes from the integration along the branch cuts around the point $h_1 = 0$. The following integral needs to be evaluated:

$$\mathcal{L}^{>}_{3,c1}(m) = \int_{\Gamma_0} d\beta\, e^{jk_3 r\sin\beta + jk_3[2(m+1)H_2 - z - z']\cos\beta} \times \sin^{5/2}\beta[\mathcal{F}_1^{+}(\beta) - \mathcal{F}_1^{-}(\beta)] \tag{18a}$$

$$\mathcal{K}^{>}_{3,c1}(m) = \int_{\Gamma_0} d\beta\, e^{jk_3 r\sin\beta + jk_3[2(m+1)H_2 - z - z']\cos\beta} \times \sin^{3/2}\beta\cos\beta[F_1^{+}(\beta) - F_1^{-}(\beta)] \tag{18b}$$

where

$$\begin{bmatrix}\mathcal{F}_1^{\pm}(\beta)\\ F_1^{\pm}(\beta)\end{bmatrix} = (1 \mp \mathcal{R}_3^{c1}e^{j2h_3z'})\{e^{-j2h_3(H_2-z)} \times [1 + (\mathcal{R}_1^{c1})^{\pm1}\mathcal{R}_2^{c1}e^{j2h_2H_1}] + (\mathcal{R}_2^{c1} + (\mathcal{R}_1^{c1})^{\pm1}e^{j2h_2H_1}]\} \times [\mathcal{R}_3^{c1}(\mathcal{R}_2^{c1} + (\mathcal{R}_1^{c1})^{\pm1}e^{j2h_2H_1}) + (\mathcal{R}_1^{c1})^{\pm1}\mathcal{R}_2^{c1}e^{j2(h_2H_1 - h_3H_2)}]^m. \tag{19}$$

To analytically evaluate the integrals (19), we expand the integration function about $\beta = \beta_{c1}$ and keep the first-order terms of both phase and amplitude functions. Since the major contribution to the integral comes from the immediate neighborhood of β_{c1}, we have

$$\begin{aligned}\begin{bmatrix}G\\ C\end{bmatrix} &= \begin{bmatrix}\mathcal{F}_1^{+}(\beta) - \mathcal{F}_1^{-}(\beta)\\ \mathcal{F}_1^{+'}(\beta) - \mathcal{F}_1^{-'}(\beta)\end{bmatrix}\\ &= \begin{bmatrix}P\\ B\end{bmatrix}\{[a\mathcal{R}_1^{c1} + b][c\mathcal{R}_1^{c1} + d]^m - [a(\mathcal{R}_1^{c1})^{-1} + b][c(\mathcal{R}_1^{c1})^{-1} + d]^m\}\\ &= P[a\mathcal{R}_1^{c1} + b][c\mathcal{R}_1^{c1} + d]^m - [a(\mathcal{R}_1^{c1})^{-1} + b] \times [c\mathcal{R}_1^{c1} + d]^m + [a(\mathcal{R}_1^{c1})^{-1} + b][c\mathcal{R}_1^{c1} + d]^m - [a(\mathcal{R}_1^{c1})^{-1} + b][c(\mathcal{R}_1^{c1})^{-1} + d]^m\}\\ &\approx [\mathcal{R}_1^{c1} - (\mathcal{R}_1^{c1})^{-1}]P\{a[c\mathcal{R}_1^{c1} + d]^m + [a(\mathcal{R}_1^{c1})^{-1} + b](mc)[c\mathcal{R}_1^{c1} + d]^{m-1}\}\end{aligned} \tag{20}$$

where

$$P = 1 - \mathcal{R}_3^{c1}e^{j2h_3z'} \tag{21a}$$

$$B = 1 + \mathcal{R}_3^{c1}e^{j2h_3z'} \tag{21b}$$

$$a = [1 + \mathcal{R}_2^{c1}e^{-j2h_3(H_2-z)}]e^{j2h_2H_1} \tag{21c}$$

$$b = \mathcal{R}_2^{c1} + e^{-j2h_3(H_2-z)} \tag{21d}$$

$$c = (\mathcal{R}_3^{c1} + \mathcal{R}_2^{c1}e^{-j2h_3H_2})e^{j2h_2H_1} \tag{21e}$$

$$d = \mathcal{R}_2^{c1}\mathcal{R}_3^{c1}. \tag{21f}$$

In (21), the reflection coefficients around the point $\beta = \beta_{c1}$ is no longer those given in (7) where λ in h_i is arbitrary. They are the specific values corresponding to $\lambda = k_1$ as given by

$$\mathcal{R}_2^{c1} = \frac{\sqrt{n_2^2 - n_1^2} - n_2^2\sqrt{1 - n_1^2}}{\sqrt{n_2^2 - n_1^2} + n_2^2\sqrt{1 - n_1^2}},$$

$$\mathcal{R}_3^{c1} = \frac{n_4^2\sqrt{1 - n_1^2} - \sqrt{n_4^2 - n_1^2}}{n_4^2\sqrt{1 - n_1^2} + \sqrt{n_4^2 - n_1^2}}.$$

At about $\beta = \beta_{c1}$, we have

$$[\mathcal{R}_1^{c1} - (\mathcal{R}_1^{c1})^{-1}] = -\frac{4n_1^2\sqrt{n_2^2 - \sin^2\beta}\,n_2^2\sqrt{n_1^2 - \sin^2\beta}}{n_2^4(n_1^2 - \sin^2\beta) - n_1^4(n_2^2 - \sin^2\beta)}. \tag{22}$$

So (20) becomes

$$\begin{bmatrix}G\\ C\end{bmatrix} = [a(c+d)^m + (mc)(a+b)(c+d)^{m-1}]\begin{bmatrix}P\\ B\end{bmatrix} \times \frac{4n_1^2\sqrt{n_2^2 - \sin^2\beta}\,n_2^2\sqrt{n_1^2 - \sin^2\beta}}{n_1^4(n_2^2 - \sin^2\beta) - n_2^4(n_1^2 - \sin^2\beta)}. \tag{23}$$

Since the time-dependence $e^{-j\omega t}$ is utilized, we therefore let

$$\beta - \beta_{c1} = js \tag{24}$$

so that we further have

$$\begin{aligned}n_1^2 - \sin^2\beta &= -2\sin\beta_{c1}\cos\beta_{c1}(\beta - \beta_{c1})\\ &= -(2jn_1\cos\beta_{c1})s\end{aligned} \tag{25a}$$

$$\sqrt{n_1^2 - \sin^2\beta} = \sqrt{2n_1\cos\beta_{c1}}e^{-j\pi/4}\sqrt{s}. \tag{25b}$$

It is noted that when the integral is evaluated from A to B, the value of s should change from ∞ to zero.

Thus, near $s = 0$, (23) may be approximated by

$$\begin{bmatrix}G\\ C\end{bmatrix} = [a(d-c)^m + (mc)(b-a)(d-c)^{m-1}]\begin{bmatrix}P\\ B\end{bmatrix} \times \frac{4n_2^2}{n_1}\sqrt{\frac{2\cos\beta_{c1}}{n_1(n_2^2 - n_1^2)}}e^{-j\pi/4}\sqrt{s}. \tag{26}$$

Since the exponential factor in (18) can be approximated by

$$\begin{aligned}j\phi &= jk_3\{r\sin\beta + [2(m+1)H_2 - z - z']\cos\beta\}\\ &= jk_3\{r\sin\beta_{c1} + [2(m+1)H_2 - z - z']\cos\beta_{c1}\}\\ &\quad + jk_3\{r\cos\beta_{c1} - [2(m+1)H_2 - z - z']\sin\beta_{c1}\}\\ &\quad \cdot(\beta - \beta_{c1})\\ &= jk_1r + jk_3\sqrt{1 - n_1^2}[2(m+1)H_2 - z - z']\\ &\quad - \{k_3\sqrt{1 - n_1^2}r - k_1[2(m+1)H_2 - z - z']\}s\end{aligned} \tag{27}$$

we can express (18) as

$$\begin{aligned}\mathcal{L}^{>}_{3,c1}(m) = &-j4n_2^2n_1\sqrt{\frac{2(1 - n_1^2)^{1/2}}{n_2^2 - n_1^2}}\,e^{-j\pi/4}\\ &\times e^{jk_1r + jk_3[2(m+1)H_2 - z - z']\sqrt{1 - n_1^2}}\\ &\times P[a(d-c)^m + (mc)(b-a)\\ &\cdot(d-c)^{m-1}] \times \int_0^{\infty}\sqrt{s}\\ &\cdot e^{-\{k_3\sqrt{1 - n_1^2}r - k_1[2(m+1)H_2 - z - z']\}s}\,ds\end{aligned} \tag{28a}$$

$$\mathcal{K}^{>}_{3,c1}(m) = -j4n_2^2\sqrt{\frac{2(1-n_1^2)^{3/2}}{n_2^2-n_1^2}}\,e^{-j\pi/4} \times e^{jk_1r+jk_3[2(m+1)H_2-z-z']\sqrt{1-n_1^2}} \times B[a(d-c)^m+(mc)(b-a) \cdot(d-c)^{m-1}] \times \int_0^\infty \sqrt{s} \cdot e^{-\{k_3\sqrt{1-n_1^2}r-k_1[2(m+1)H_2-z-z']\}s}\,ds \quad (28b)$$

Using the integral

$$\int_0^\infty \sqrt{s}e^{-\alpha s}\,ds = \frac{1}{2\alpha}\sqrt{\frac{\pi}{\alpha}}$$

we finally get

$$\mathcal{L}^{>}_{3,c1}(m) = -j2n_2^2n_1\sqrt{\frac{2\pi(1-n_1^2)^{1/2}}{n_2^2-n_1^2}}e^{-j\pi/4} \times e^{jk_1r+jk_3[2(m+1)H_2-z-z']\sqrt{1-n_1^2}} \times P[a(d-c)^m+(mc)(b-a) \cdot(d-c)^{m-1}] \times \{k_3\sqrt{1-n_1^2}r - k_1[2(m+1)H_2-z-z']\}^{-3/2} \quad (29a)$$

$$\mathcal{K}^{>}_{3,c1}(m) = -j2n_2^2\sqrt{\frac{2\pi(1-n_1^2)^{3/2}}{n_2^2-n_1^2}}e^{-j\pi/4} \times e^{jk_1r+jk_3[2(m+1)H_2-z-z']\sqrt{1-n_1^2}} \times B[a(d-c)^m+(mc)(b-a) \cdot(d-c)^{m-1}] \times \{k_3r\sqrt{1-n_1^2} - k_1[2(m+1)H_2-z-z']\}^{-3/2}. \quad (29b)$$

Substituting (29) back to (12), we finally obtained the expression of the lateral wave that propagates along the upper air-canopy interface. It is given by

$$\begin{bmatrix}E^{>V}_{3z,c1}\\ E^{<V}_{3z,c1}\end{bmatrix} = -\frac{\omega\mu_0k_3P_z}{8\pi}\sqrt{\frac{2}{\pi k_3r}}\,e^{-j(\pi/4)} \cdot\sum_{m=0}^{\infty}\begin{bmatrix}\mathcal{L}^{>}_{3,c1}(m)\\ \mathcal{L}^{<}_{3,c1}(m)\end{bmatrix} \quad (30a)$$

$$\begin{bmatrix}E^{>H}_{3z,c1}\\ E^{<H}_{3z,c1}\end{bmatrix} = \frac{\omega\mu_0k_3}{8\pi}\,P_x\cos\phi\sqrt{\frac{2}{\pi k_3r}}e^{-j(\pi/4)} \cdot\sum_{m=0}^{\infty}\begin{bmatrix}\mathcal{K}^{>}_{3,c1}(m)\\ \mathcal{K}^{<}_{3,c1}(m)\end{bmatrix}. \quad (30b)$$

B. Lateral Wave Along Canopy–Trunk Interface

In a similar fashion, we can obtain the lateral wave expressions contributed by both the horizontal and vertical polarization moments. They are provided as follows:

$$\begin{bmatrix}E^{>V}_{3z,c2}\\ E^{<V}_{3z,c2}\end{bmatrix} = -\frac{\omega\mu_0k_3P_z}{8\pi}\sqrt{\frac{2}{\pi k_3r}}\,e^{-j(\pi/4)} \cdot\sum_{m=0}^{\infty}\begin{bmatrix}\mathcal{L}^{>}_{3,c2}(m)\\ \mathcal{L}^{<}_{3,c2}(m)\end{bmatrix} \quad (31a)$$

$$\begin{bmatrix}E^{>H}_{3z,c2}\\ E^{<H}_{3z,c2}\end{bmatrix} = \frac{\omega\mu_0k_3}{8\pi}\,P_x\cos\phi\sqrt{\frac{2}{\pi k_3r}}\,e^{-j(\pi/4)} \cdot\sum_{m=0}^{\infty}\begin{bmatrix}\mathcal{K}^{>}_{3,c2}(m)\\ \mathcal{K}^{<}_{3,c2}(m)\end{bmatrix} \quad (31b)$$

where

$$\mathcal{L}^{>}_{3,c2}(m) = j2n_2\sqrt{2\pi}e^{jk_2r+jk_3[2(m+1)H_2-z-z']\sqrt{1-n_2^2}} \times e^{-j\pi/4}[1-\mathcal{R}_3^{c2}e^{j2h_3z'}](-1)^me^{-j2mh_3H_2} \times\left\{\frac{n_1^2}{\sqrt{n_1^2-n_2^2}}\,(1-n_2^2)^{1/4} \cdot[1-e^{j2h_3(z-H_2)}]-(1-n_2^2)^{-1/4} \cdot[1+e^{j2h_3(z-H_2)}]\right\}\times\{k_3r\sqrt{1-n_2^2} - k_2[2(m+1)H_2-z-z']\}^{-(3/2)} \quad (32a)$$

$$\mathcal{K}^{>}_{3,c2}(m) = \frac{\sqrt{1-n_2^2}}{n_2}\,\frac{1+\mathcal{R}_3^{c2}e^{j2h_3z'}}{1-\mathcal{R}_3^{c2}e^{j2h_3z'}}\,\mathcal{L}^{>}_{3,c2}(m). \quad (32b)$$

The reflection coefficient $\mathcal{R}_3^{c2}$ is given by

$$\mathcal{R}_3^{c2} = \frac{k_4^2\sqrt{k_3^2-k_2^2}-k_3^2\sqrt{k_4^2-k_2^2}}{k_4^2\sqrt{k_3^2-k_2^2}+k_3^2\sqrt{k_4^2-k_2^2}}. \quad (33)$$

C. Lateral Wave Along Ground–Trunk Interface

The expressions of the lateral wave propagating along the ground–trunk interface are derived and given below:

$$\begin{bmatrix}E^{>V}_{3z,c4}\\ E^{<V}_{3z,c4}\end{bmatrix} = -\frac{\omega\mu_0k_3P_z}{8\pi}\sqrt{\frac{2}{\pi k_3r}}\,e^{-j(\pi/4)} \cdot\sum_{m=0}^{\infty}\begin{bmatrix}\mathcal{L}^{>}_{3,c4}(m)\\ \mathcal{L}^{<}_{3,c4}(m)\end{bmatrix} \quad (34a)$$

$$\begin{bmatrix}E^{>H}_{3z,c4}\\ E^{<H}_{3z,c4}\end{bmatrix} = \frac{\omega\mu_0k_3}{8\pi}\,P_x\cos\phi\sqrt{\frac{2}{\pi k_3r}}\,e^{-j(\pi/4)} \cdot\sum_{m=0}^{\infty}\begin{bmatrix}\mathcal{K}^{>}_{3,c4}(m)\\ \mathcal{K}^{<}_{3,c4}(m)\end{bmatrix} \quad (34b)$$

where

$$\begin{bmatrix}\mathcal{L}^{>}_{3,c4}(m)\\ \mathcal{K}^{>}_{3,c4}(m)\end{bmatrix} = j2n_4\sqrt{\frac{2\pi}{(1-n_4^2)^{1/2}}}\begin{bmatrix}1\\ \sqrt{1-n_4^2}/n_4\end{bmatrix} \times e^{jk_4r+jk_3[2(m+1)H_2-z-z']\sqrt{1-n_4^2}-j\pi/4} \times[(\mathcal{R}_2^{c4}+\mathcal{R}_1^{c4}e^{j2h_2H_1}) +(1+\mathcal{R}_1^{c4}+\mathcal{R}_2^{c4}e^{j2h_2H_1})e^{j2h_3(z-H_2)}] \cdot\{\mp e^{j2h_3z'}\times[(\mathcal{R}_2^{c4}+\mathcal{R}_1^{c4}e^{j2h_2H_1}) +\mathcal{R}_1^{c4}\mathcal{R}_2^{c4}e^{j2h_2H_1-j2h_3H_2}]^m +m(\mathcal{R}_2^{c4}+\mathcal{R}_1^{c4}e^{j2h_2H_1}) \times(1\mp e^{j2h_3z'})[(\mathcal{R}_2^{c4}+\mathcal{R}_1^{c4}e^{j2h_2H_1}) +\mathcal{R}_1^{c4}\mathcal{R}_2^{c4}e^{j2h_2H_1-j2h_3H_2}]^{m-1}\} \times\{k_3r\sqrt{1-n_4^2} - k_4[2(m+1)H_2-z-z']\}^{-(3/2)}. \quad (35)$$

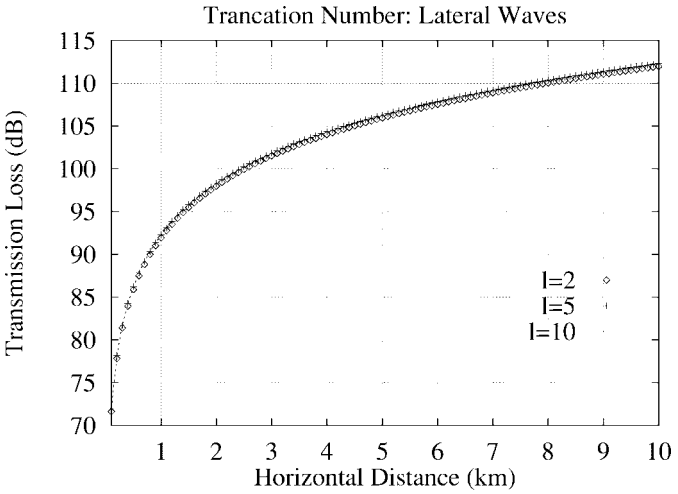

Fig. 4. Consideration of iteration convergence for three-interface lateral waves.

The reflection coefficients are correspondingly given by

$$\mathcal{R}_1^{c4} = \frac{k_2^2\sqrt{k_1^2-k_4^2} - k_1^2\sqrt{k_2^2-k_4^2}}{k_2^2\sqrt{k_1^2-k_4^2} + k_1^2\sqrt{k_2^2-k_4^2}} \tag{36a}$$

$$\mathcal{R}_2^{c4} = \frac{k_3^2\sqrt{k_2^2-k_4^2} - k_2^2\sqrt{k_3^2-k_4^2}}{k_3^2\sqrt{k_2^2-k_4^2} + k_2^2\sqrt{k_3^2-k_4^2}}. \tag{36b}$$

D. Convergence Consideration

Similar to that of the direct and multireflected waves, the convergence of the lateral waves along the three interfaces is also examined. The lateral waves at an operating frequency of 100 MHz are computed within the range of 0.1–10 km, as shown in Fig. 4, where the iteration is truncated at numbers of $m = 2, 5$, and 10, respectively. It is found that the first six terms (i.e., $m = 5$) have led to an accuracy of less than 10^{-5}% relative error. The iteration of the lateral waves converges quite rapidly.

V. Complex Images: Least-Squares Prony's Method

A. Remaining Integral

Quasi-dynamic images contributed dominant field in the near-radiating zone. However, to employ these images only to represent the field in the near-radiating region is not accurate enough. To improve the accuracy, the Prony's method [25] provides the supplementary contributions due to the complex images.

For the fields in near zone, the lateral waves propagating along the three interfaces can be ignored. Thus, the remaining field in (9) after extracting the contributions due to the quasi-dynamic images becomes

$$E_{3z,ci}^{>} = -\frac{\omega\mu_0}{8\pi k_3^2}\int_{-\infty}^{\infty}\lambda^2\, d\lambda\, F(\lambda) \left(jP_x\cos\phi H_1^{(1)}(\lambda r) + P_z\frac{\lambda}{h_3}H_0^{(1)}(\lambda r)\right)e^{jh_3(z-z')} \tag{37}$$

where

$$F(\lambda) = \frac{\Phi_+^{>}(\lambda)}{D_3^V}e^{-jh_3(z-z')} - \frac{\phi_3^{>}}{\mathcal{D}_3^V} \tag{38a}$$

$$\phi_3^{>} = [1+\mathcal{R}_3^V e^{j2h_3z'}]\{[1+\mathcal{R}_1^V\mathcal{R}_2^V e^{j2h_2H_1}] + [\mathcal{R}_2^V + \mathcal{R}_1^V e^{j2h_2H_1}]e^{j2h_3(H_2-z)}\} \tag{38b}$$

$$\mathcal{D}_3^V = 1+\mathcal{R}_1^V\mathcal{R}_2^V e^{j2h_2H_1} - [\mathcal{R}_2^V + \mathcal{R}_1^V e^{j2h_2H_1}]e^{j2h_3H_2}. \tag{38c}$$

B. Least-Squares Prony's Method

To calculate the remaining integral, as given above, the least-squares Prony's method provides an efficient way [24] although numerical evaluation is also a choice; however, its speed is relatively slower, as discussed by [26].

The least-squares Prony's method approximates a complex function of real argument to a series of complex exponents [25]. To do so, a conformal mapping given by

$$h_i = k_i\left[-jt + \left(1-\frac{t}{T_0}\right)\right], \qquad 0 \le t \le T_0 \tag{39}$$

is normally applied. This mapping transforms the complex variable h_i ($\in [k_i, -jk_iT_0]$) into a real variable t ($\in [0, T_0]$) in the parameter function in (39). The choice of T_0 in the λ plane depends upon the behavior of the integrand in (37). It has been tested that T_0 is usually taken as 15 although the choice of T_0 such as five and ten is quite arbitrary [23].

Taking the least squares of the following function:

$$\Delta = \left|F(\lambda) - \sum_{i=1}^{N} A_i e^{B_i t}\right|^2 \tag{40}$$

we may obtain the coefficients A_i and B_i where the number N of the sets of the coefficients is taken as three or larger. Therefore, the function $F(\lambda)$ can be approximated to

$$F(\lambda) = \sum_{i=1}^{N} A_i e^{B_i t} = \sum_{i=1}^{N} a_i e^{b_i h_3} \tag{41}$$

where

$$a_i = A_i e^{B_iT_0/(1+jT_0)} \tag{42a}$$

$$b_i = B_iT_0/[k_i(1+jT_0)]. \tag{42b}$$

The asymptotic field components $E_{3z}^{>V}$ and $E_{3z}^{>H}$ in (12) due to the complex images are obtained as follows:

$$E_{3z,ci}^{>V} = -\frac{\omega\mu_0 P_z}{4\pi}\sqrt{\frac{k_3}{|k_3|}}\, e^{-j(5\pi/8)}\sum_{i=1}^{N}\frac{e^{jk_2R_i(z,z')}}{\sqrt{rR_i(z,z')}} \tag{43a}$$

$$E_{3z,ci}^{>H} = -\frac{\omega\mu_0 P_x\cos\phi}{4\pi}\sqrt{\frac{k_3}{|k_3|}}\, e^{-j(5\pi/8)} \times\sum_{i=1}^{N}\frac{z-z'-jb_i}{r}\frac{e^{jk_3R_i(z,z')}}{\sqrt{rR_i(z,z')}} \tag{43b}$$

where

$$R_i(z,z') = \sqrt{r^2+[z-z'-jb_i]^2}. \tag{44}$$

TABLE I
DIELECTRIC PARAMETERS OF THE TYPICAL FOUR-LAYERED FOREST MODEL

Layer #	Region Extent	Perm. ϵ_r	Cond. σ (mS/m)
I	$H_1 + H_2 \le z < \infty$	1	0
II	$H_1 \le z \le H_1 + H_2$	40	0.3
III	$0 \le z \le H_1$	35	0.1
IV	$-\infty < z \le 0$	50	100

H_1 and H_2 are usually chosen to be 10 m and 20 m.

The fields $E_{3z,ci}^{<(H,V)}$ in the region $z \le z'$ are obtainable by simply interchanging the roles of (z, z') and (z', z).

It is found numerically that the contribution due to the complex images is very much smaller as compared with those of the quasi-dynamic images and the lateral waves along the three interfaces. Therefore, this contribution is not included in the computation although the method for accounting the complex images is provided for both understanding and possible future usage.

VI. TRANSMISSION LOSS DUE TO FOREST

Total field due to the quasi-dynamic images and the complex images is the sum of the following two contributions, i.e.,

$$E_{\text{total}} = E_{\text{total}}^{V} + E_{\text{total}}^{H} \tag{45}$$

where

$$E_{\text{total}}^{V} = E_{3z,qd}^{V} + E_{3z,c1}^{V} + E_{3z,c2}^{V} + E_{3z,c3}^{V} + E_{3z,ci}^{V} \tag{46a}$$

$$E_{\text{total}}^{H} = E_{3z,qd}^{H} + E_{3z,c1}^{H} + E_{3z,c2}^{H} + E_{3z,c3}^{H} + E_{3z,ci}^{H}. \tag{46b}$$

Each of the terms in the right-hand side of (46) has already been given in order by (16), (30), (31), (34), and (43), respectively.

To illustrate the radio wave attenuation due to the forest, we adopt the following dielectric parameters in Table I for the canopy and trunk layers and ground. It is pointed out that these typical parameters are employed for the convenience of future comparison between the computed results and the existing data published elsewhere. For various forest environments such as average forest, dense forest, and rain forest, the dielectric parameters differ from one set to another. Many other parameters can also be used for the comparison [13] once they are recorded in the realistic experiment.

The formula used in the computation of the transmission loss is given by

$$L(\text{dB}) = 36.57 + 20\log_{10}[f(\text{GHz})] + 20\log_{10}\left|\frac{E_0}{E}\right| \tag{47}$$

where f is the operating frequency in gigahertz and E_0 is the field in the absence of the forest. To accurately compute this field, the effects of the ground must be taken into account. In this paper, this field is calculated from (16) where the permittivities of the canopy and trunk layers are made equal to those in free-space, i.e., $\epsilon_2 = \epsilon_3 = \epsilon_0$. In the following computations, it is assumed that the parameters tabulated in Table I are utilized and $z = 15$ m, $z' = 10$ m, and $\alpha = -5.71°$.

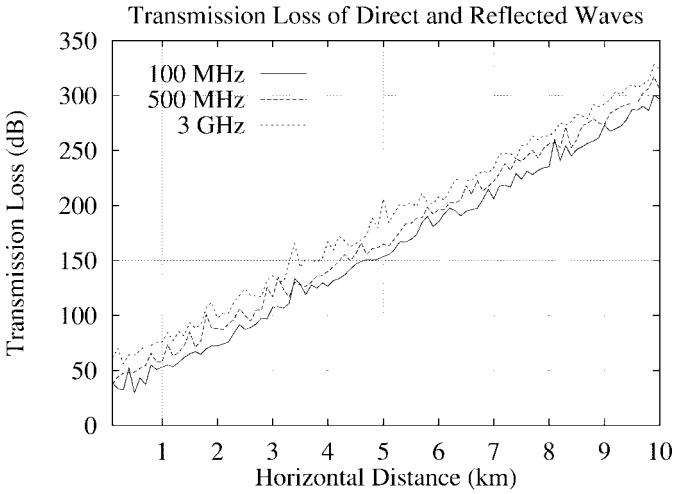

Fig. 5. Transmission loss of direct and multireflected waves against horizontal distance at frequencies of 100 MHz, 500 MHz, and 3 GHz.

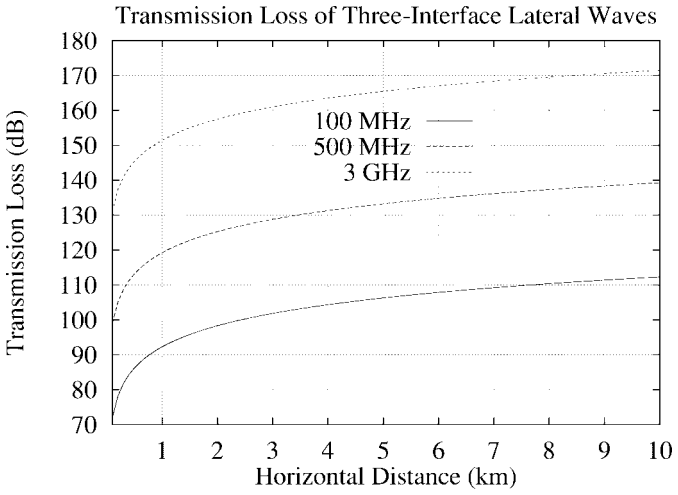

Fig. 6. Transmission loss of three-interface lateral waves against horizontal distance at frequencies of 100 MHz, 500 MHz, and 3 GHz.

To show the effect of the canopy and trunk layers, the transmission losses of the direct and multireflected waves are computed within the range of 0.1–10 km at frequencies of 100 MHz, 500 MHz, and 3 GHz. The results are plotted in Fig. 5. It is evident in Fig. 5 that the loss becomes large as the operating frequency increases. Also, it is seen that the attenuation is almost a linearly increasing function of horizontal distance. It becomes too high for the receiver to receive its signal as the transmitter and the receiver are separated at a distance of 5 km or longer.

The lateral waves along the three interfaces are also computed numerically. As shown earlier in Fig. 4, the computation converges fast and only six terms are needed to achieve a relative error of 10^{-5}%. Fig. 6 depicts the transmission loss variation against the horizontal distance at a frequency of 100 MHz, 500 MHz, and 3 GHz. Numerical computation demonstrates that the lateral wave propagating along the

upper side of the air-canopy interface dominates the overall contributions of the three-interface lateral waves when the horizontal distance is large. The lateral waves along the canopy-trunk interface and the trunk-ground interface occupy a very small percentage of the overall contribution, and can, hence, be ignored. A conclusion similar to that of the direct and multireflected waves can be drawn for the three-interface lateral waves, that is, the transmission loss increases with the operating frequency at a known distance r or with the horizontal distance at a given frequency f. A different observation is that the transmission loss of the lateral waves varies slower than that of the direct and reflected waves.

To gain an insight into the contributions due to individual groups of waves to the total fields, Fig. 7 illustrates the transmission losses of: 1) the overall waves; 2) the direct and multireflected waves; and 2) the three-interface lateral waves at frequencies of 100 MHz, 500 MHz, and 3 GHz. It is obvious in Fig. 7 that the direct and multihop reflected waves dominate the overall electric fields in the near zone where the horizontal distance r is small, say, about 3 km for the waves at 100 MHz, about 4 km for the waves at 500 MHz, and about 5 km for the waves at 3 GHz. However, the lateral waves, in fact, the lateral wave along the upper side of the air–canopy interface, plays an important role in contributing the overall waves as the horizontal distance becomes large, for instance, larger than 3 km for the waves at 100 MHz, about 4 km for the waves at 500 MHz, and about 5 km for the waves at 3 GHz.

To demonstrate the variation of transmission loss with respect to the operating frequency ranging from 100 MHz to 3 GHz, Fig. 8 depicts such configurations at horizontal distances of 0.5, 1, and 5 km, respectively. It is evident that the transmission loss is an increasing function of the operating frequency. Also, it is obvious that the transmission loss of the direct and reflected waves fluctuates intensely with the frequency; but such a fluctuation for the lateral waves becomes faint with the frequency although existing. Generally, the conclusion drawn from the theoretical analysis here is almost the same as that from the experimental observations [27]. However, the direct comparison with the experimental data in [27] is impossible so far due to the lack of the detailed permittivity of the canopy and trunk layers in [27]. It is known that different types of forest have different forest densities and, therefore, different dielectric characteristics.

VII. Concluding Remarks

In this paper, a novel analysis of the radio waves propagating along mixed paths inside a four-layered forest model is carried out. Closed-form representation of the $\hat{z}$ component of the electric fields is obtained within two regions, i.e., $0 \leq z \leq z'$ and $z' \leq z \leq H$ in the layer III. Radio wave attenuation is also calculated numerically. Contributions of various waves along different paths are discussed and a comparison of contributions due to various modes is made.

Analytical derivation shows that the original integral can be replaced by four integrals—one along the steepest descent contour and the other along three branch cuts. Corresponding formulas are obtained, representing the direct wave and mul-

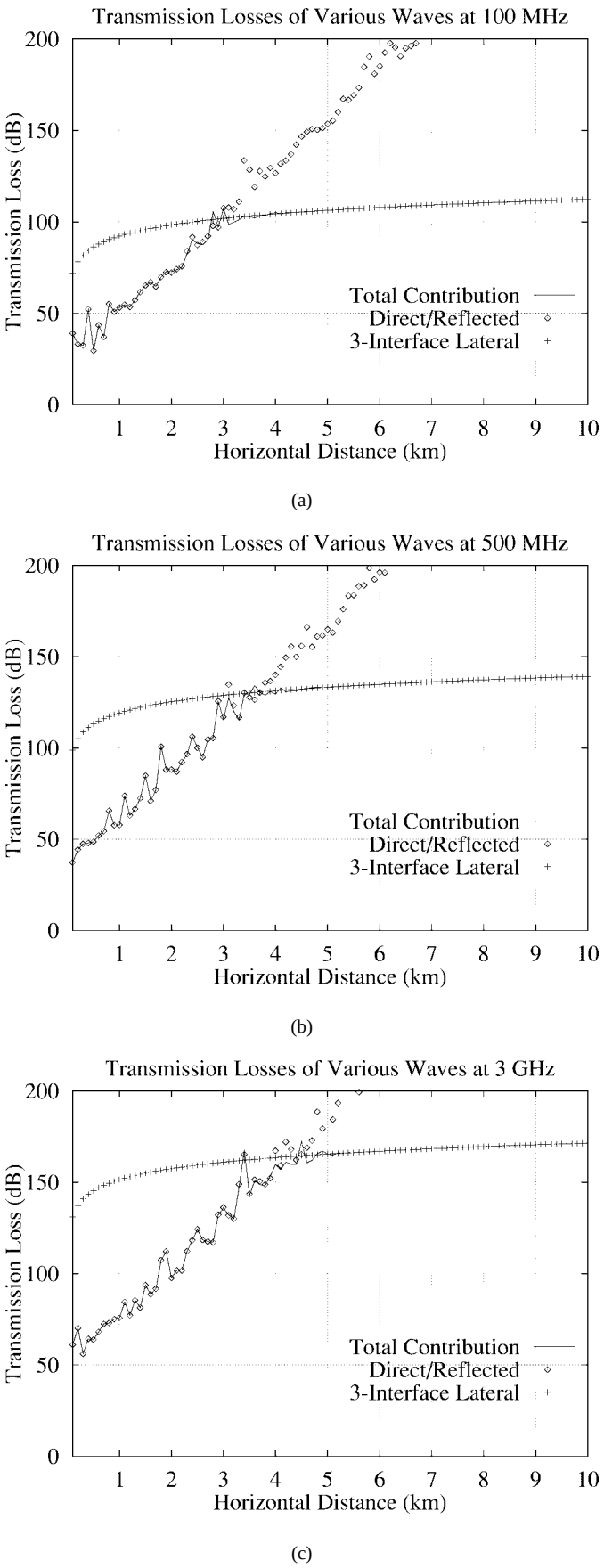

Fig. 7. Comparison of transmission losses of: 1) the overall waves; 2) the direct and multireflected waves; and 3) the three-interface lateral waves at frequencies of 100 MHz, 500 MHz, and 3 GHz.

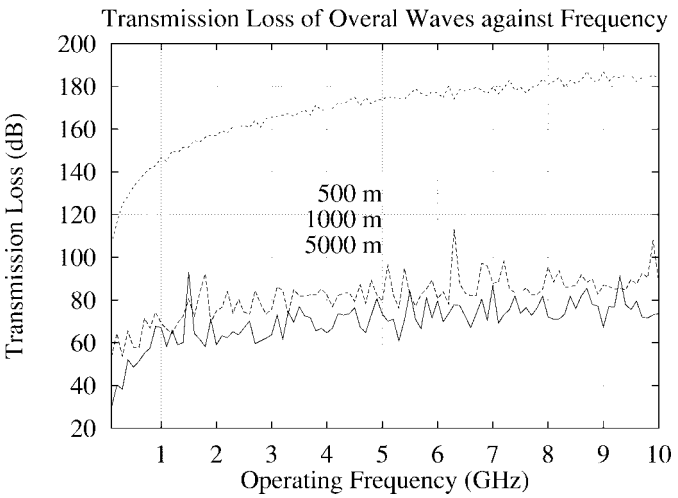

Fig. 8. Transmission losses of the overall waves against operating frequency at a horizontal distance of 0.5, 1, and 5 km.

tireflected waves and three lateral waves along three interfaces. The conventional way to derive the direct wave and multireflected waves is to make use of saddle-point technique. In this paper, a method that combines the saddle-point technique and the quasi-static approximation is employed to obtain a series of expressions. Of this series, the zeroth order term, i.e., the first term for $m = 0$, stands for the direct wave; the other terms denote the multiple reflected waves and the hop number is just the summation index number. Also, it is found that accuracy is highly improved and the validity condition of the saddle-point technique becomes relaxed and is not strictly obeyed. The lateral waves are obtained by evaluating the integrals along the respective branch cuts around the poles and three lateral waves are derived and found to be those propagating along three interfaces. Of the three lateral waves, the dominant wave is the one propagating along the upper side of the air-canopy interface.

In lossless media, the direct wave due to the point source radiation is always the major contribution. In the lossy forest medium, it is found that this wave also plays an important role in the near-zone field within a horizontal distance range of about 3 km depending upon the operating frequency. The reflected waves also contribute to the overall guided waves considerably. Numerical computation shows that the iteration of the direct and multihop reflected waves can be truncated to 40 within an expected truncation error. This implies that the multireflected waves with hop number less than 40 still contribute to the overall guided waves. However, in the far zone the electric field is dominated by the lateral wave along the first interface. The guided waves play an important role in contributing the total field in the near zone, say, with a horizontal distance of about 3 km. However, the lateral wave propagating along the upper side of the air-canopy interface dominates the total field in the far zone where the horizontal distance is larger than 3 km for the waves at 100 MHz, 4 km at 5 MHz, and 5 km at 3 GHz. Also, in the far zone, the lateral waves along the canopy-trunk and trunk-ground interfaces can, as compared with the lateral wave along the air-canopy interface, be neglected.

An important observation is that all the direct and multireflected waves contributed by images and obtained from quasi-static approximation and the saddle point evaluations are proportional to e^{ik_3R}/R while the lateral waves obtained from the branch cut evaluations are proportional to e^{ik_0R}/R^2. Therefore, when the distance R between transmitter and receiver is small, the contribution of images to the total field becomes the dominant. Besides, all the waves also decay exponentially except for the lateral wave along the upper side of the air-canopy interface. Since the direct and reflected waves propagate inside the *lossy* canopy-trunk dielectric waveguide and two lateral waves with the canopy-medium and ground-medium wave numbers propagate along the upper-side interface of canopy–trunk and the lower-side interface of the trunk–ground, the decay of the waves due to the images and the two lateral waves in the lossy media are much faster than that of the lateral wave propagating along the upper side of air–canopy interface when R becomes large. Therefore, such a lateral wave at a large distance R plays an especially important role in contributing to the total field.

APPENDIX
DOMINANT WAVES DUE TO REAL DIPOLE AND QUASI-DYNAMIC IMAGES

Physically, (16) consists of direct wave and multireflected waves. The dominant contributions of these waves are extracted subsequently.

A. Direct Wave from the Real Source

Since the direct wave is always used to calculate the field in the absence of the lossy canopy and trunk layers, it is an important measure to account for the transmission loss of the radio waves that propagate through the forest medium. When the distance between the transmitter and the receiver is small, the direct wave in the forest is the dominant wave. Applying the saddle-point evaluation, we find that the integral consisting of $\mathcal{K}_3(m)$ vanishes so that $E_{3z}^{>} \simeq E_{3z}^{>V}$ and $E_{3z}^{<} \simeq E_{3z}^{<V}$. The direct wave due to the real dipole antenna is then given by

$$E_{\text{direct}} = -\frac{\omega\mu_0}{4\pi}\left(P_z - P_x\cos\phi\,\frac{z-z'}{r}\right) \times \sqrt{\frac{k_3}{|k_3|}}\,e^{-j(5\pi/8)}\,\frac{e^{jk_3R'_-(0,z,z')}}{\sqrt{rR'_-(0,z,z')}}. \quad \text{(A.1)}$$

It can be seen from this expression that the field is symmetrical for the source point z' and observation point z. Exchanging the source and field points does not, as expected, affect the result, which is physically reasonable.

B. One-Hop Reflected Waves Due to Quasi-Dynamic Images

There exist three different cases for the one-hop reflected waves. The waves excited by the dipole could be reflected directly by either the first, second, or third interface. The one-hop reflected waves due to each of the three interfaces are

given in the order of the interfaces by

$$E^{\mathrm{I}}_{\mathrm{reflected}} = -\frac{\omega\mu_0}{4\pi}\,\mathcal{R}^s_1 e^{j2\sqrt{k_2^2-k_3^2}H_1}\,\frac{e^{jk_3R_-(0,z,z')}}{\sqrt{rR_-(0,z,z')}}\,\sqrt{\frac{k_3}{|k_3|}} \times e^{-j(5\pi/8)}\left(P_z - P_x\cos\phi\,\frac{2H_2-z-z'}{r}\right) \tag{A.2a}$$

$$E^{\mathrm{II}}_{\mathrm{reflected}} = -\frac{\omega\mu_0}{4\pi}\,\mathcal{R}^s_2\,\frac{e^{jk_3R_-(0,z,z')}}{\sqrt{rR_-(0,z,z')}}\,\sqrt{\frac{k_3}{|k_3|}}\,e^{-j(5\pi/8)} \times\left(P_z - P_x\cos\phi\,\frac{2H_2-z-z'}{r}\right) \tag{A.2b}$$

$$E^{\mathrm{III}}_{\mathrm{reflected}} = -\frac{\omega\mu_0}{4\pi}\,\mathcal{R}^s_3\,\frac{e^{jk_3R'_+(0,z,z')}}{\sqrt{rR'_+(0,z,z')}}\,\sqrt{\frac{k_3}{|k_3|}}\,e^{-j(5\pi/8)} \times\left(P_z - P_x\cos\phi\,\frac{z+z'}{r}\right). \tag{A.2c}$$

The physical geometries of image excitations are shown in Fig. 9. The wave arriving at the observation point is reflected once by the first, second or third interface. The reflection coefficients have been used in the field expressions. The fields in (A.2a)–(c) represent the waves excited by the images due to the first, second, and third interfaces, respectively. Also, a rule must be followed to derive individual contribution; that is, when an image due to one interface is concerned, other interfaces are considered to be transparent for wave propagation. This is similar to the rule in the image theory that when the wave due to an image is concerned, the perfect conductor ground must be removed.

C. Two-Hop Reflected Waves from Quasi-Dynamic Images

In a similar fashion, the two-hop reflected fields due to the interfaces are expressed as follows:

$$E^{\mathrm{I\&II}}_{\mathrm{reflected}} = -\frac{\omega\mu_0}{4\pi}\,\mathcal{R}^s_1\mathcal{R}^s_2 e^{j2\sqrt{k_2^2-k_3^2}H_1}\,\frac{e^{jk_3R'_-(0,z,z')}}{\sqrt{rR'_-(0,z,z')}} \times\sqrt{\frac{k_3}{|k_3|}}\,e^{-j(5\pi/8)} \cdot\left(P_z - P_x\cos\phi\,\frac{2H_2+z-z'}{r}\right) \tag{A.3a}$$

$$E^{\mathrm{II\&III}}_{\mathrm{reflected}} = -\frac{\omega\mu_0}{4\pi}\,\mathcal{R}^s_3\mathcal{R}^s_2\,\frac{e^{jk_3R_+(0,z,z')}}{\sqrt{rR_+(0,z,z')}} \times\sqrt{\frac{k_3}{|k_3|}}\,e^{-j(5\pi/8)} \cdot\left(P_z - P_x\cos\phi\,\frac{2H_2-z+z'}{r}\right) \tag{A.3b}$$

$$E^{\mathrm{I\&III}}_{\mathrm{reflected}} = -\frac{\omega\mu_0}{4\pi}\,\mathcal{R}^s_3\mathcal{R}^s_1 e^{j2\sqrt{k_2^2-k_3^2}H_1}\,\frac{e^{jk_3R_+(0,z,z')}}{\sqrt{rR_+(0,z,z')}} \times\sqrt{\frac{k_3}{|k_3|}}\,e^{-j(5\pi/8)} \cdot\left(P_z - P_x\cos\phi\,\frac{2H_2-z+z'}{r}\right). \tag{A.3c}$$

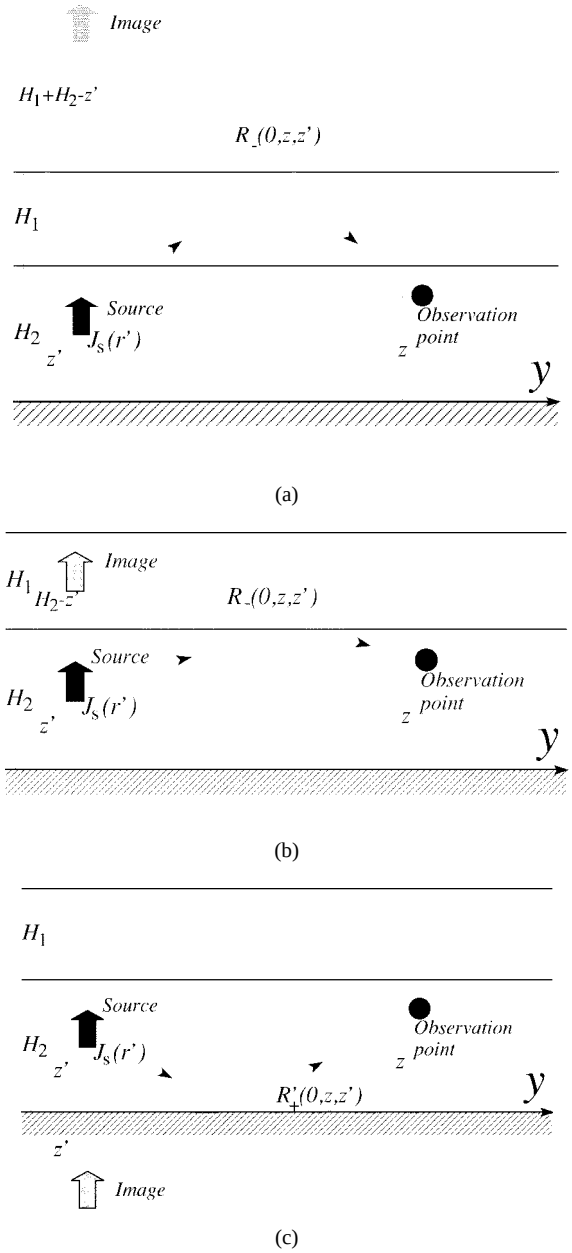

Fig. 9. One-hop reflected waves from interfaces between (a) air–canopy, (b) canopy–trunk, and (c) trunk–ground.

As can be seen from the representations of the reflected fields, two reflection coefficients are used for different images produced due to the corresponding interfaces.

D. Three-Hop Reflected Waves from Quasi-Dynamic Images

A single three-hop reflected mode exists in the expression of electric field contributed by the quasi-dynamic images. This mode is written as

$$E^{\mathrm{I\&II\&III}}_{\mathrm{reflected}} = -\frac{\omega\mu_0}{4\pi}\,\mathcal{R}^s_3\mathcal{R}^s_1\mathcal{R}^s_2 e^{j2\sqrt{k_2^2-k_3^2}H_1} \cdot\frac{e^{jk_3R'_+(0,z,z')}}{\sqrt{rR'_+(0,z,z')}} \times\sqrt{\frac{k_3}{|k_3|}}\,e^{-j(5\pi/8)} \cdot\left(P_z - P_x\cos\phi\,\frac{z+z'}{r}\right). \tag{A.4}$$

It can be seen from the mode expression containing three reflection coefficients that the quasi-static image should be the one due to first the trunk–ground interface, then the air–canopy interface, and finally the canopy–trunk interface.

E. Images' Characteristics and Their Geometries

As discussed earlier, the interfaces that are not concerned can be considered to be transparent to the wave propagation. Different orders n of images can be obtained from the number n of interfaces. The real source with zeroth order (nil) image produces the direct wave propagating directly from the transmitter to the receiver. The first-order images produce the waves reflected once by the air-canopy, the canopy-trunk, or the trunk-ground interface. The propagation mechanisms of the single-reflected waves can be described by drawing directly the propagation path between the image and the receiver, as shown in Fig. 9.

However, the mechanisms of the double-reflected waves cannot be completely represented by means of graphics. The propagation path between the image due to the air-canopy and canopy-trunk interfaces and the observation point cannot be graphically drawn. However, separation of the reflection coefficient at the canopy-trunk interface $\mathcal{R}_2^s$ into unity and the transmission coefficient $(1+\mathcal{T}_2^s)$ can make the graphical illustration possible. Also, it seems from the expressions of $\mathcal{R}_1^s\mathcal{R}_2^s$, $\mathcal{R}_3^s\mathcal{R}_2^s$, and $\mathcal{R}_3^s\mathcal{R}_1^s$ that the order of two reflection coefficients does not matter. As a matter of fact, it does. This can be seen from the phase expressions of the fields that there is only a possibility for the waves being twice reflected. The waves excited by the images cannot be included into the expressions given by (A.3a)–(c). They are included in the higher order modes as $m=1$.

Similar phenomena to those in the second-order images can also be found in the third order images. The three reflection coefficients may form six different combinations, i.e., $\mathcal{R}_1^s\mathcal{R}_2^s\mathcal{R}_3^s$, $\mathcal{R}_1^s\mathcal{R}_3^s\mathcal{R}_1^s$, $\mathcal{R}_2^s\mathcal{R}_3^s\mathcal{R}_1^s$, $\mathcal{R}_2^s\mathcal{R}_1^s\mathcal{R}_3^s$, $\mathcal{R}_3^s\mathcal{R}_1^s\mathcal{R}_2^s$, and $\mathcal{R}_3^s\mathcal{R}_2^s\mathcal{R}_1^s$, respectively, corresponding to different vertical distances in phases of $(2H_1-z-z')$, $(2H_1+4H_2-z-z')$, $(2H_1+4H_2-z-z')$, $(2H_1+z+z')$, $(2H_1+z+z')$, and $(2H_1-z-z')$. The field in (A.4) represents only two of them. The other four can be found from the higher order modes.

Besides the above, it is evident that $R_\pm(m,z,z')$ and $R'_\pm(m,z,z')$ denote only the path lengths of multireflected waves along the waveguide between two interfaces: canopy-trunk and trunk-ground. The optical path in the canopy region is not counted in the distances $R_\pm(m,z,z')$ and $R'_\pm(m,z,z')$. However, it has also been considered and expressed in terms of the phase form: $e^{j2\sqrt{k_2^2-k_3^2}H_1}$.

ACKNOWLEDGMENT

The authors would like to thank M.-H. Ng for his Mathematica and Fortran programs to carry out the numerical computation and J.-H. Koh for his careful proofreading. One of the authors, L.-W. Li would like to thank the reviewers for their helpful suggestions on improving the paper's presentation.

REFERENCES

[1] T. Tamir and L. B. Felsen, "On lateral waves in slab configurations and their relation to other wave types," *IEEE Trans. Antennas Propagat.*, vol. AP-13, p. 410, 1965.
[2] T. Tamir, "On radio-wave propagation in forest environments," *IEEE Trans. Antennas Propagat.*, vol. AP-15, pp. 806–817, Nov. 1967.
[3] J. R. Wait, "Influence of a subsurface insulating layer on ground wave propagation," *IEEE Trans. Antennas Propagat.*, vol. AP-14, pp. 755–759, June 1966.
[4] D. L. Sachs and P. J. Wyatt, "A conducting slab model for electromagnetic propagation within a jungle medium," *Radio Sci.*, vol. 3, pp. 125, 1968.
[5] D. Dence and T. Tamir, "Radio loss of lateral waves in forest environments," *Radio Sci.*, vol. 4, p. 307, 1969.
[6] G. N. Tsandoulas, "Excitation of a ground dielectric slab by a horizontal dipole," *IEEE Trans. Antennas Propagat.*, vol. AP-17, pp. 156–161, Mar. 1969.
[7] T. Tamir, "Radio waves propagation along mixed paths in forest environments," *IEEE Trans. Antennas Propagat.*, vol. AP-25, pp. 471–477, July 1977.
[8] G. P. S. Cavalcante and A. J. Giardola, "Optimization of radio communication in media with three layers," *IEEE Trans. Antennas Propagat.*, vol. AP-31, pp. 141–145, Jan. 1983.
[9] L. W. Li and P. N. Jiao, "Calculation of path loss in forest-communication," *J. China Inst. Commun.*, vol. 8(6), pp. 20–25, 1987.
[10] G. P. S. Cavalcante, D. A. Rogers, and A. J. Giardola, "Radio loss in forests using a model with four layered media," *Radio Sci.*, vol. 18, pp. 691–695, 1983.
[11] H. X. Lian, "UHF lateral wave loss in forests modeled by four-layered media," *Acta Electron. Sinica*, vol. 14, no. 5, pp. 12–20, 1986.
[12] L. W. Li and P. N. Jiao, "Solution of the electromagnetic field in a forest model with four layered media," *Chinese J. Radio Sci.* (in Chinese) [or *J. Guizhou Univ.–Natural Sci.* (in English)], vol. 1(2) [or 6(3) and 7(1) (in two parts)], pp. 10–25 [or 24–31 and 41–52], 1986 (and 1989 and 1990, respectively).
[13] S. S. Seker and A. Schneider, "Stochastic model for pulsed radio transmission through stratified forests," *Proc. Inst. Elect. Eng.*, vol. 134, pt. H, pp. 361–368, 1987.
[14] S. S. Seker, "Radio pulse transmission along mixed paths in a stratified forest," *Proc. Inst. Elect. Eng.*, vol. 136, pt. H, pp. 13–18, 1989.
[15] L. W. Li, "Wave propagation and communication within random inhomogeneous media," Ph.D. dissertation, Inst. Electron. Acad. Sinica, Beijing, 100080 China, with China Res. Inst. Radiowave Propagat., Xinxiang, Henan, 453003, China, Oct. 1990.
[16] R. W. P. King, M. Owens, and T. T. Wu, "Properties of lateral electromagnetic fields and their application," *Radio Sci.*, vol. 21, p. 13, 1986.
[17] T. T. Wu and R. W. P. King, "Lateral waves: A new formula and interference patterns," *Radio Sci.*, vol. 17, p. 13, 1982.
[18] ———, "Lateral waves: New formulas for E_r and E_ϕ," *Radio Sci.*, vol. 17, p. 532, 1982.
[19] W. Y. Pan, "Measurement of lateral waves along a three-layered medium," *IEEE Trans. Antennas Propagat.*, vol. AP-34, pp. 267–271, Feb. 1986.
[20] J. M. Dunn, "Lateral wave propagation in a three-layered medium," *Radio Sci.*, vol. 21, p. 787, 1986.
[21] L. W. Li, P. S. Kooi, M. S. Leong, and T. S. Yeo, "On the eigenfunction expansion of dyadic Green's function in planarly stratified media," *J. Electromagn. Waves Applicat.*, vol. 8, no. 6, pp. 663–678, June 1994.
[22] A. Ishimaru, *Electromagnetic Wave Propagation, Radiation, and Scattering*. Englewood Cliffs, NJ: Prentice-Hall, 1991.
[23] Y. L. Chow, J. J. Yang, D. G. Fang, and G. E. Howard, "A closed-form spatial Green's function for the thick microstrip substrate," *IEEE Trans. Microwave Theory Tech.*, vol. 39, pp. 588–592, Mar. 1991.
[24] M. I. Aksun and R. Mittra, "Derivation of closed-form spatial Green's functions for a general microstrip geometry," *IEEE Trans. Microwave Theory Tech.*, vol. 40, pp. 2055–2062, Nov. 1992.
[25] S. L. Marple, *Digital Spectral Analysis with Applications*. Englewood Cliffs, NJ: Prentice-Hall, 1987.
[26] J. J. Yang, Y. L. Chow, and D. G. Fang, "Discrete complex images of a three-dimensional dipole above and within a lossy ground," *Proc. Inst. Elect. Eng.*, vol. 138, pt. H, no. 4, pp. 319–326, 1991.
[27] R. K. Tewari, S. Swarup, and M. N. Roy, "Radio wave propagation through rain forrests of india," *IEEE Trans. Antennas Propagat.*, vol. 38, pp. 433–449, Apr. 1990.

Le-Wei Li (S'91–M'92–SM'96) received the B.Sc. degree (physics) from Xuzhou Normal University, Xuzhou, China, the M.Eng.Sc degree from the China Research Institute of Radiowave Propagation (CRIRP), Xinxiang, China, and the Ph.D. degree (electrical engineering) from Monash University, Melbourne, Australia, in 1984, 1987, and 1992, respectively.

From 1987 to 1989, he was with the Ionospheric Propagation Laboratory at the CRIRP and in 1989 he was with the Henan-Province Association of Science and Technology, Zhengzhou, China. In 1992, he worked at La Trobe University (jointly with Monash University), Melbourne, Australia, as a Research Fellow. Since 1992 He has been with the Department of Electrical Engineering at the National University of Singapore, where he is currently a Senior Lecturer. His current research interests include electromagnetic theory, radio wave propagation and scattering in various media, microwave propagation and scattering in tropical environment, and antenna radiation.

Dr. Li received the Science and Technology Achievement Awards by the CRIRP in 1987 from the Ionospheric Propagation Laboratory at the CRIRP, the Best Paper Award from the Chinese Institute of Communications in 1990, and the Prize Paper Award from the Chinese Institute of Electronics in 1991. He was selected to receive a Ministerial Science & Technology Advancement Award by Ministry of Electronic Industries, China, in 1995 and a National Science & Technology Advancement Award by National Science & Technology Committee, China, in 1996.

Tat-Soon Yeo (M'80–SM'93) received the B.Eng. (honors) and M.Eng. degrees from the National University of Singapore, in 1979 and 1981, respectively, and the Ph.D. degree from the University of Canterbury, New Zealand, in 1985.

Since 1985, he has been with the Electrical Engineering Department of the National University of Singapore, where he is currently an Associate Professor. His current research interests are in wave propagation and scattering, antennas, and numerical techniques.

Dr. Yeo received the 1997 Defence Science Organization (DSO) R&D Award from DSO National Laboratories, Singapore, in 1997. He is also the chairman of the MTT/AP/EMC joint chapter, Singapore IEEE Section.

Pang-Shyan Kooi (M'75) received the B.Sc. degree (electrical engineering) from the National Taiwan University, Taipei, the M.Sc. (Tech) degree (electrical engineering) from the University of Manchester Institute of Science and Technology (UMIST), Manchester, U.K., and the D.Phil. degree (engineering science) from Oxford University, U.K., in 1963, 1961, and 1970, respectively.

Since 1970, he has been with the Electrical Engineering Department of the National University of Singapore, where he is currently a Professor of electrical engineering. His current research interests are microwave and millimeter-wave circuits and antennas.

Mook-Seng Leong (M'81) received the B.Sc. degree in electrical engineering (first class honors) and the Ph.D. degree in microwave engineering from the University of London, U.K., in 1968 and 1971, respectively.

He is currently a Professor of electrical engineering at the National University of Singapore. He is a member of the editorial board for *Microwave and Optical Technoloogy Letters* and *Wireless Mobile Communications*. His main research interests include antenna and waveguide boundary-value problems and semiconductor characterization using the spreading resistance profiling (SRP) technique.

Dr. Leong is a member of the Massachusetts Institute of Technology (MIT)-based Electromagnetic Academy and a Fellow of the Institution of Electrical Engineers, London, U.K. He received the 1996 Defence Science Organization (DSO) R&D Award from DSO National Laboratories, Singapore, in 1996.